



# Single photon detection with amorphous silicon-based microchannel plates: A Monte Carlo model

Janina Löffler<sup>a,\*</sup>, Jonathan Thomet<sup>a</sup>, Samira Frey<sup>a</sup>, Christophe Ballif<sup>a,b</sup>, Nicolas Wyrsch<sup>a</sup>

<sup>a</sup> Photovoltaics and Thin-Film Electronics Laboratory, Institute of Electrical and Micro Engineering (IEM), Ecole Polytechnique Fédérale de Lausanne (EPFL), Neuchâtel, Switzerland

<sup>b</sup> CSEM, Centre Suisse d'Electronique et Microtechnique, Neuchâtel, Switzerland

## ARTICLE INFO

### Keywords:

Microchannel plate  
Single photon detection  
Secondary electron emission  
Monte Carlo model  
a-Si:H  
High secondary electron emissive layers

## ABSTRACT

Microchannel plates based on amorphous silicon have the inherent capability to overcome the existing spatial and temporal resolution limitations of single photon detectors. A Monte Carlo model-based study is presented here that serves to exploit their full potential. The dynamics of electron multiplication throughout the microchannels in the presence of an electric field is modelled based on electron emission models and experimental measurements. The geometrical limits for suitable amplification and the expected time resolution of amorphous silicon based microchannel plates are presented. Furthermore, the model is implemented in a finite element method simulator to estimate electron multiplication gain and time response for channels with various geometries. With gains above 1000 and timing jitters below 3 ps that are shown for selected geometries, AMCPs enable ultrafast measurements for medical applications and single photon detection.

## 1. Introduction

Amorphous silicon-based microchannel plates (AMCPs) are a promising alternative to current generation single photon detectors. More specifically, AMCPs can improve the spatial resolution in pixel detectors to pixel sizes on the order of a few  $\mu\text{m}$ . They can also be monolithically integrated with readout electronics, therefore enabling collection efficiencies approaching 100% depending on the shape of the microchannels. A first generation of AMCPs with channels having a moderate (below 14) aspect ratio (AR) was demonstrated by Franco et al. [1] to be used as electron multipliers. The fabrication of AMCPs, in contrast to microchannel plates (MCPs), mainly consists of the following two steps: a thick a-Si:H layer is deposited by plasma-enhanced chemical vapour deposition (PECVD), followed by deep reactive ion etching (DRIE) to form the channels. Unlike MCPs, AMCPs provide bulk conductivity and do not require activation at the channel walls to sustain AMCP operation. To date, AMCPs have been fabricated with channel lengths up to 90  $\mu\text{m}$ , channel diameters as small as 2.7  $\mu\text{m}$  and an AR of up to 23 [2]. With further improvements in the fabrication process, ARs of up to 50 are within immediate reach.

In a photon counting detector with AMCPs, incident photons are converted into electrons by a photocathode. For single photon detection AMCPs need to produce a minimum number of about  $10^3$  electrons per incident electron for the readout electronics [3]. Depending on the application, the timing resolution (i.e. timing jitter) is equally important. In modern time-of-flight (TOF) positron emission tomography (PET)

detectors, for instance, it is crucial to reduce the coincidence timing resolution (CTR) to below 10 ps [4]. This means the intrinsic timing jitter of the photon detector should be below that value as well. Both the charge multiplication gain and timing jitter are therefore key output parameters for optimization. The model presented in this paper allows computation of both quantities, paving the way for the development of high CTR and high gain AMCPs for use in single-photon detection.

There are two main types of modelling frameworks in the literature that describe the multiplication process in MCP channels. On the one hand, transmission line models have been developed, such as the one presented by Guidicotti et al. [5] and, on the other hand Monte Carlo (MC) models have been developed, as for instance by Tremsin et al. [6] and by Kruschwitz et al. [7]. While transmission line models describe the MCP response to an incident current, the MC method is used to model the response of MCPs to single electrons allowing for the calculation of statistical variations in gain and timing jitter. Advanced MCP models include a time dependent single channel MC model developed by Kruschwitz et al. [7] and a fast Monte Carlo method by Shymanska et al. [8]. The latter is used to calculate parallel multiplication paths in multiple channels while minimizing calculation cost.

The model presented in this paper builds on the framework of previous MC models. Electrons are accelerated by an electric field inside a microchannel and at each interaction with the channel wall secondary electrons can be emitted. By following the electron trajectories throughout the channel and their interaction with the channel wall,

\* Corresponding author.

E-mail address: [janina.loeffler@hevs.ch](mailto:janina.loeffler@hevs.ch) (J. Löffler).

the number of output electrons and timing statistics are calculated. While the former MCP models are calibrated through experimental MCP results, we pre-calibrated the electron interaction dynamics in the AMCP model. This was done by depositing a thin layer of a-Si:H followed by independently testing the electron emission dynamics on this thin layer. In the absence of AMCP experimental results, these measurements were critical in creating a more accurate model. Furthermore, unlike the existing models, elastic scattering was measured independently in the experimental process, and inelastic scattering was also included in our model. Additionally, a novel finite element model is presented in this work that enables calculation of electron dynamics inside arbitrary AMCP geometries, electric and magnetic fields.

The AMCP model presented in this paper allows for the determination of optimal geometries of cylindrical channels, the limits of AMCP gain and timing resolution, and the impact of arbitrary non-cylindrical channel geometries on AMCP performance. In addition, electron dynamics inside the channel (i.e. the interaction mechanism), the number of impacts along the channel wall and the arrival energy distribution of the electrons are reported. The impact of highly emissive coatings (e.g. Al<sub>2</sub>O<sub>3</sub> and MgO) deposited by atomic layer deposition (ALD) method on the performance of AMCPs is investigated as well. These highly emissive materials can further improve the AMCPs gain, as they generate a higher number of secondary electrons than a-Si:H at each interaction. The goal of this work is to first present a basis on which to design application specific AMCPs, as the results provide guidelines to fabricate optimal geometries on the one hand and to design suitable readout electronics on the other. Furthermore, the model can be used to predict the impact of various materials and geometries on AMCP performance.

## 2. Electron-wall interaction

Electron interaction with the AMCP channel wall is the fundamental process leading to multiplication in the AMCP channel and is the basis of the Monte Carlo model presented in here. Primary electron interaction with the channel wall can lead to secondary emission. The simulation of each electron trajectory then allows one to calculate the output gain and timing jitter in a single AMCP channel or in the complete geometry of AMCP arrays. The secondary electron emission at each primary electron interaction point is a stochastic process and needs to be described with a probabilistic model [9]. The outcomes of this model are the average number of emitted electrons, their emission energy distribution and their angular distribution. The former two depend on the incident electron energy, and the incident angle. These incident values are determined by the electron emission energy and angle, the electric field inside the AMCP channel and the channel geometry. Electron-electron interaction is neglected in our model.

### 2.1. Total electron emission yield and secondary electron emission

The average number of emitted electrons per incident electron is given by the total electron emission yield,  $\sigma$ . The total emission yield depends on the incident electron energy  $E_{in}$  and angle  $\theta$ . The incident electron can be backscattered with a probability  $P_{BS}$ , that depends on the incident electron's energy. In case an electron is not backscattered it enters the material and can create secondary electrons. At low energies,  $\sigma$  can be below 1. However, the measured value of  $\sigma$  is an average number where both backscattering and secondary emission processes happen at the same time. The secondary yield  $\delta$  needs to be corrected for single events. In a single event, an elastically backscattered electron cannot contribute to secondary emission. Therefore, the  $\delta$  used in the AMCP model has been corrected for mutual exclusivity of backscattering and secondary emission. The elastic backscattering yield  $\eta_e$  denotes the relative number of electrons that are backscattered elastically and

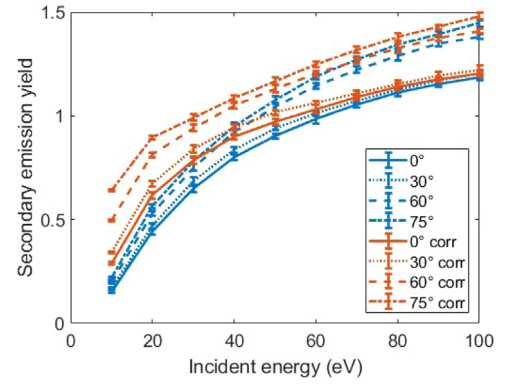


Fig. 1. Correction of the secondary yield  $\delta$  for single events shown for a-Si:H at different incident angles. The experimental secondary electron yield (blue) was measured as a sum of elastic backscattering events and secondary emission. In a single event these processes are exclusive. Considering that secondary electrons can only be created by primary electrons that have not been backscattered, the effective secondary yield for the AMCP model is the corrected secondary yield (red).

$\eta_{ie}$  is the inelastic backscattering yield which will be discussed further below. The corrected secondary yield is therefore:

$$\delta(E_{in}, \theta) = (\sigma(E_{in}, \theta) - \eta_e(E_{in}, \theta) - \eta_{ie}(E_{in}, \theta)) \cdot \frac{1}{1 - \eta_e(E_{in}, \theta)}, \quad (1)$$

where  $\eta_e = P_{BS} \cdot \sigma$  and  $\eta_{ie} = P_{IBS} \cdot \sigma$ . The backscattering probabilities  $P_{BS}$  and  $P_{IBS}$  have been measured on flat a-Si:H layers, with and without the high secondary emissive material Al<sub>2</sub>O<sub>3</sub> [10]. Fig. 1 shows the measured and corrected secondary yield values of hydrogenated amorphous (a-Si:H) silicon for various angles of incidence. The backscattering yield can be described using the following equation:

$$\eta_e(E_{in}) = a \exp(-b \cdot E_{in}) + c, \quad (2)$$

where  $a$ ,  $b$  and  $c$  are constant fitting values of an exponential decay function with  $\eta_e(0) = a + c = 1$ , assuming 100% backscattering at 0 eV incident energy [11]. The third process contributing to  $\sigma$  is inelastic backscattering with the yield  $\eta_{ie}$ , calculated as  $\eta_{ie} = P_{IBS} \cdot \sigma$ . The inelastic backscattering probability  $P_{IBS}$  has been derived by Löffler [10]. As the dependence of inelastic backscattering on the energy is small, we assume a fixed value for the inelastic backscattering yield of  $\eta_{ie} = 0.2$  for electron energies above 50 eV. The relative contribution of  $\eta_{ie}$  to  $\sigma$  is small and therefore negligible. However, these electrons can have significantly higher emission energies than secondary electrons. Thus, the present model also includes inelastic backscattering.

### 2.2. Energetic and angular distribution

The energy distributions for a-Si:H and Al<sub>2</sub>O<sub>3</sub> coated surfaces were measured for low incident energies, and the parametrizations derived from the measurements presented by Löffler [10] were used. In our model, Lambert's cosine law describes the angular distribution of emitted electrons. A more accurate description of the angular distribution depends on the surface chemistry at the emission point [12]. Thus, the spherical emission angles,  $\theta_{SE}$  and  $\varphi_{SE}$ , were drawn from the following distributions:

$$P(\theta_{SE}) = \frac{1}{\pi} (1 + \cos(2\theta_{SE})) \quad (3)$$

where  $\theta_{SE}$  is the emission angle relative to the surface normal, between 0 and  $\pi/2$ . The azimuthal angle,  $\varphi_{SE}$ , is independent of this distribution and can take all values between 0 and  $2\pi$

$$P(\varphi_{SE}) = \frac{1}{2\pi}. \quad (4)$$

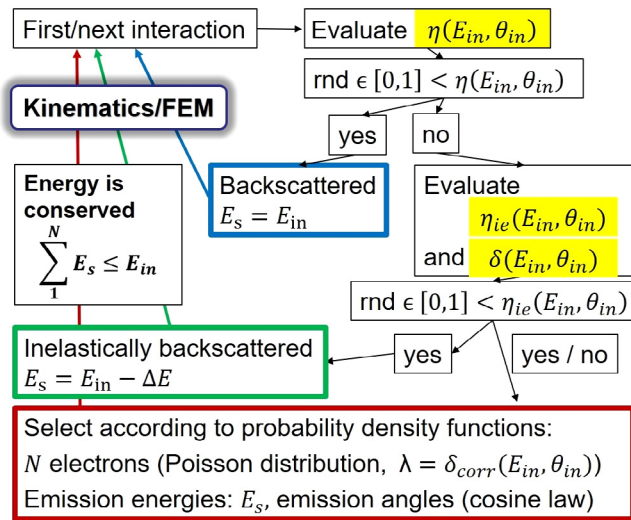


**Fig. 2.** Process steps for AMCP Monte Carlo Models. For each interaction, the stochastic process of secondary emission is modelled, using the elastic backscattering yield  $\eta(E_{in}, \theta_{in})$ , the inelastic backscattering yield  $\eta_{ie}(E_{in}, \theta_{in})$  and the secondary emission yield  $\delta(E_{in}, \theta_{in})$ . As a result of the interaction, the electron is either backscattered elastically or a number of  $N$  secondary electrons are emitted and/or the electron is inelastically backscattered while the energy is conserved, i.e. the sum of all emitted electron energies is less than or equal to the incident electron's energy. All electrons created/the electron backscattered at the interaction point with emission energies  $E_i$  and their emission angles, are/is given to the kinematic or finite element model (FEM) to calculate their next interaction point. Of course, it can be possible that the electron is completely absorbed; in this case the simulation process stops for that electron.

### 3. Model details

In this section, we present the models that were used to calculate the single electron response of AMCP channels and arrays with various geometries. The basis of the models is a probabilistic description of electron emission at each interaction point of the incident electron. For an electron impinging on the AMCP channel wall, the electron emission model shown in Fig. 2 is applied. If the incident electron with energy  $E_{in}$  is not backscattered, it can create secondary electrons with an expected value  $\delta$  of its Poisson distribution. Additionally, the electron can be inelastically backscattered with a probability  $\eta_{ie}$ . The sum of all the emission energies,  $E_s(i)$ , is chosen from the emission energy probability distribution with the condition  $\sum_{i=1}^N E_s(i) \leq E_{in}$ . Of course, in these models, a non-zero probability exists that an electron is completely absorbed, which could happen at any interaction point of an electron with the channel wall; in that case the simulation process stops for this particular electron.

As mentioned above, both a kinematic model and a finite element model (FEM) were developed in the current work. In the kinematic model, an AMCP channel is represented by a perfect cylinder with diameter  $d$  and length  $l$ . The secondary electrons accelerated by an assumed constant electric field travel along the channel until they either hit the channel wall at a distance  $d \cdot \cos \beta$  or exit the channel (see Fig. 3). The direction of these secondary electrons and the distance they can travel are determined by their emission energy,  $E_s$ , and emission angles,  $\alpha_0, \beta$ . In the FEM instead, the electric field inside the channel is not necessarily constant. Any arbitrary channel geometry can be chosen and the electric potential is calculated at each point of the FEM mesh.

In the kinematic model, the calculation starts at the first interaction point, where the (true) primary electron reaches the channel wall (see Fig. 4). Here, the distance between the consecutive interactions depends on the incident angle. As the height of the first interaction has a greater impact on the AMCP channel output compared to the incident angle  $\theta$ , a fixed incident angle was defined that led to a first interaction point height distribution in the interval of  $\left[ l, l - \frac{d}{\tan \theta} \right]$ .

In the FEM, the electron dynamics are defined by the geometry and electric potential in each individual point of the mesh. We used the particle tracing module of Comsol Multiphysics® v.5.3., where the movement is governed by the Newtonian formulations from classical mechanics. The model was solved for time steps of 2 ps between 0 ps and 80 ps. We chose a physics-controlled mesh with a minimum element size of 200 nm and a maximum size of 4  $\mu\text{m}$ . The first primary electron angle and impact height resulted from electron emission from a photocathode and the consequent acceleration through the electric field between the photocathode the AMCP channel surface. Examples for the electric field at the top of AMCP channels are shown in 2D in Fig. 13.

Surface chemistry and surface structure are the factors that determine electron emission in the AMCP channel. These factors depend on the AMCP fabrication process and can vary along the depth of the channel. Unfortunately, it is extremely difficult to incorporate the effect of local roughness in the secondary emission calculation as, depending on the local electric field strength, curvature has been shown to increase secondary emission [13] while shading can decrease it [14,15].

Furthermore, secondary emission depends on the availability of charges in the channel surface layer, as was highlighted by Cazaux et al. [16] and Belhaj et al. [17]. These space charge effects, acting on the secondary emission ultimately lead to pore gain saturation in conventional MCPs for high gains. For the considered diameters in the order of 1  $\mu\text{m}$  these would play a role for gains starting at  $10^5$  in MCPs [18]. Since the calculated gains are below this value, space charge effects were not considered in the present model. Additionally, the bulk conductivity of AMCPs may even increase the gain limit for pore gain saturation. A difference between MCPs and AMCPs has been observed for count rate saturation: While MCPs operated at currents above  $10^{-14}$  A [19] show count rate saturation, experimental results on AMCPs have not shown a similar trend thus far. AMCPs have been operated with a maximal input current of  $10^{-13}$  A [20]. Overall, since single incident electrons at moderate gains are considered, it is assumed that the electric field is not affected by the electron avalanche.

AMCP response to single electrons has not been measured and to date, a maximum gain of 150 has been measured for AMCPs. This could potentially lead to calculation of unrealistically high gains. To overcome this challenge, the electron emission parameters were calibrated from both thin film measurements and AMCP gain measurements. Additionally the sensitivity of AMCP gain and timing on the electron emission parameters was analysed in the following section. It is worth noting that the AMCP gain has been shown to increase for lower input fluxes [20]. Thus, the calibration used here leads to an underestimate of the expected gain for single electrons. Consequently, the results of the current model can be regarded as a lower bound for the AMCP gain in single photon detection.

### 4. Model calibration and sensitivity analysis

This section illustrates the calibration procedure for the emission parameters of the AMCP model. As mentioned, the electron emission parameters were calibrated from measurements of secondary electron emission on thin films and from gain measurements on AMCPs. In the first place, we derived all the emission parameters from the thin film measurements and then adjusted the maximum gain parameter,  $\delta_m$ , to fit AMCP gain measurements. The angular dependence of the secondary electron yield  $\delta$  is inspired from Vaughan's model [21], as shown below:

$$\delta(E, \theta) = \delta_m(\theta) \left( \frac{E}{E_m(\theta)} \exp \left[ 1 - \frac{E}{E_m(\theta)} \right] \right)^s, \quad (5)$$

where  $E$  and  $\theta$  are the incident energy and angle, respectively, and  $s$  is a positive parameter value chosen to best fit the data.  $E_m$  and  $\delta_m$  are defined as

$$E_m(\theta) = E_m(0) \left( 1 + k \frac{\theta^2}{2\pi} \right) \quad (6)$$

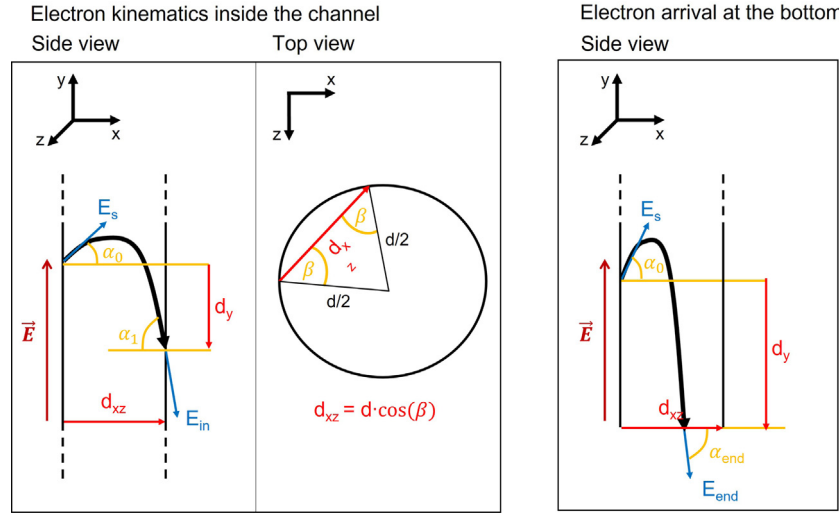


Fig. 3. Kinematic Model. Electron trajectories are modelled in a cylindrical channel with a constant electric field  $\vec{E}$ . The electron trajectory is calculated according to the emission energy  $E_s$  and angle  $\theta$ , which leads to the electron either encountering the channel wall at a distance  $d_{xz}$  or exiting the channel at the bottom.

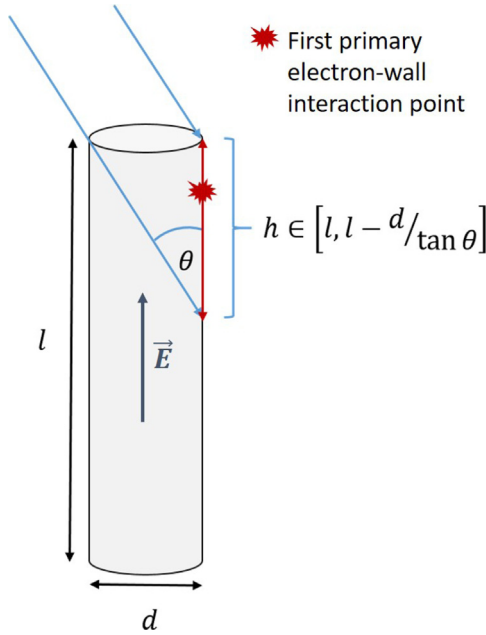


Fig. 4. Definition of the incident angle  $\theta$  and the resulting first interaction point  $h$  in the kinematic model.

and

$$\delta_m(\theta) = \delta_m(0) \left( 1 + k \frac{\theta^2}{2\pi} \right). \quad (7)$$

where  $E_m(0)$  is the energy of maximum secondary yield  $\delta_m(0)$  at normal incidence. The parameter  $k$  is a constant between 0 and 2, which indicates the surface smoothness. The calibration of  $\delta_m$  to fit the AMCP gain measurements is shown in Fig. 5. As can be observed in Fig. 5a, no single value of  $\delta_m$  could be found to represent the gain measurements at different aspect ratios. As mentioned in the previous section, the gain of AMCPs has been observed to increase for lower input flux. For this reason, we used the secondary emission parameter 'model  $\delta_m$  fit' that has been adjusted to the highest gain value. In the following sections, we use the adjusted parameters shown in Table 1.

In order to determine the impact of the electron emission parameter variation on the calculated gain and timing resolution, we analysed the expected gain and timing jitter for different secondary emission

Table 1

(a) Model parameter values for the elastic backscattering yield. The inelastic backscattering yield was approximated to be 0.2 for incident energies above 50 eV. (b) Model parameters for the secondary emission yield of a-Si:H,  $\text{AlO}_x$  and MgO, after calibration. The experimental secondary yield parameters of a-Si:H and  $\text{AlO}_x$  thin film layers are given in parenthesis. The values for MgO were fitted to the secondary yield measured by Jokela et al. [22] and the angular dependence simulated by Ivanov et al. [23]. For conventional MCPs the values for  $\text{SiO}_2$  were derived by Kruschwitz et al. [7] and Ivanov et al. [23].

(a) Elastic backscattering yield  $\eta_e$

Fit curve (Eq. (2)) for angles  $\theta \leq 85^\circ$

Material	Fit parameters		
	a	b	c
a-Si:H	0.9845	0.06005	0.0155
$\text{Al}_2\text{O}_3$	0.987	0.069	0.013
MgO	Was not calculated, we use the parameters of $\text{Al}_2\text{O}_3$		

Theoretical model of Cazaux et al. [11] is used for angles  $\theta > 85^\circ$ .

(b) Secondary emission yield  $\delta$

Empirical model [21] for  $\delta(E_m)$  (Eqs. (5)–(7))

Material	Fit constants			
	$\delta_m$	$E_m$ (eV)	k	s
a-Si:H	1.65 (1.33)	220	1.63	0.23
$\text{Al}_2\text{O}_3$	2.5 (2.68)	310	0.45	0.45
MgO	4.8	514	1.67	0.69
$\text{SiO}_2$	3–4 [7] / 5.63 [23]	300 [7] / 350 [23]	0.5–1 [7]	0.62 [7]

parameters and inelastic backscattering yield  $\eta_{ie}$ . For an AMCP channel with a diameter of 6.6  $\mu\text{m}$ , length of 90  $\mu\text{m}$  and an expected gain of 110, we varied the parameters  $s$ ,  $k$ ,  $\delta_m$  and  $\eta_{ie}$ , as shown in Fig. 6. As expected, the gain increased considerably with an increase in  $\delta_m$ , while an increase in  $\eta_{ie}$  lead to only a minor increase of the gain. Additionally, the timing jitter was slightly reduced for higher  $\delta_m$ . The shaping parameter  $s$  did not affect the gain, nor the timing jitter. An increase in the parameter  $k$  led to an increase in gain and reduced the timing jitter. Overall the shaping parameters  $s$  and  $k$  did not significantly affect the results. The variations in  $\delta_m$  modified the expected gain, but did not affect the timing jitter considerably. This sensitivity analysis indicates that even if all the secondary emission parameters are fitted from few measurements, we can predict the AMCP timing jitter and the expected lower limit of AMCP gain.

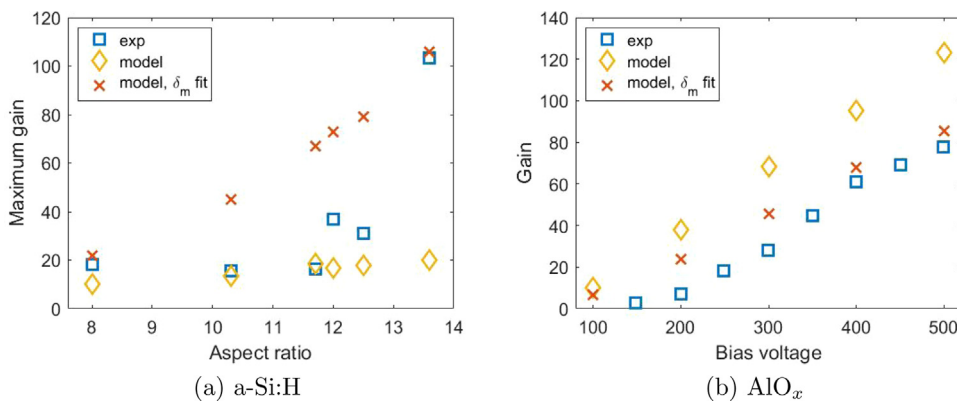


Fig. 5. (a) Gain calculated with the AMCP single channel model before (yellow) and after (orange) calibration of the maximum secondary yield at normal incidence  $\delta_m$  of a-Si:H for all measured aspect ratios at the maximum electric field they were measured with respectively (blue). (b) Gain depending on the bias voltage calculated for Al<sub>2</sub>O<sub>3</sub> before (yellow) and after (orange) calibration and compared to the experimental values (blue). Experimental values were taken from [20].

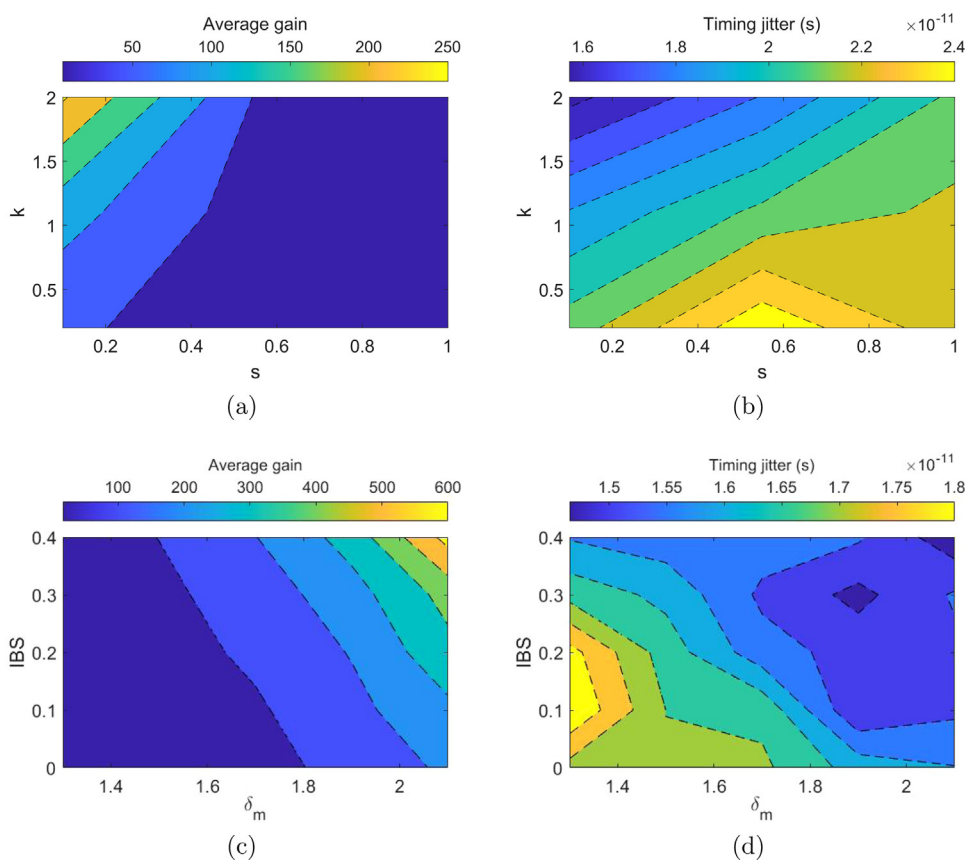


Fig. 6. The sensitivity of AMCP gain and timing jitter on four parameters is shown here for an AMCP sample with aspect ratio 13.6 and an expected gain of about 100: in (a) and (b) the effect of the secondary yield curve shaping parameters  $s$  and  $k$  is shown, in (c) and (d) the maximum secondary yield  $\delta_m$  and the additional inelastic backscattering probability IBS are shown.

### 5. Kinematic model results

This section presents an analysis of the electron multiplication inside an AMCP channel with 60  $\mu\text{m}$  length and 2  $\mu\text{m}$  diameter. This is the geometry of the highest aspect ratio AMCP that has been realized to date. Furthermore, the expected gain and timing resolution for different geometries, specifically for smaller channel diameters are presented. The results of this section can help to guide future optimization of AMCP geometries.

Using the kinematic model for a single cylindrical channel, the cumulative response of the AMCP channel to 1000 incident electrons at a channel bias voltage of 500 V, corresponding to an electric field of

8.3 V/ $\mu\text{m}$ , was calculated. a-Si:H can sustain an electric field of at least 20 V/ $\mu\text{m}$  (based on our experience) before dielectric breakdown occurs. This high dielectric breakdown limit can allow to further increase the gain and reduce the timing jitter. However, 500 V has been set as the maximum voltage for experimental gain measurements due to instrument limitations, and thus this value was used as the typical AMCP bias voltage in our analysis. In the calculations, the channel length is  $l$  and the diameter is  $d$ . The initial electrons are assumed to strike the channel at a random height between  $l$  and a height  $l - \tan(\theta)d$ , depending on the incident angle  $\theta$  of the primary electron beam and the channel diameter  $d$ .  $\theta$  is set to 30° unless mentioned otherwise. The results of our calculations are shown in Fig. 7. The

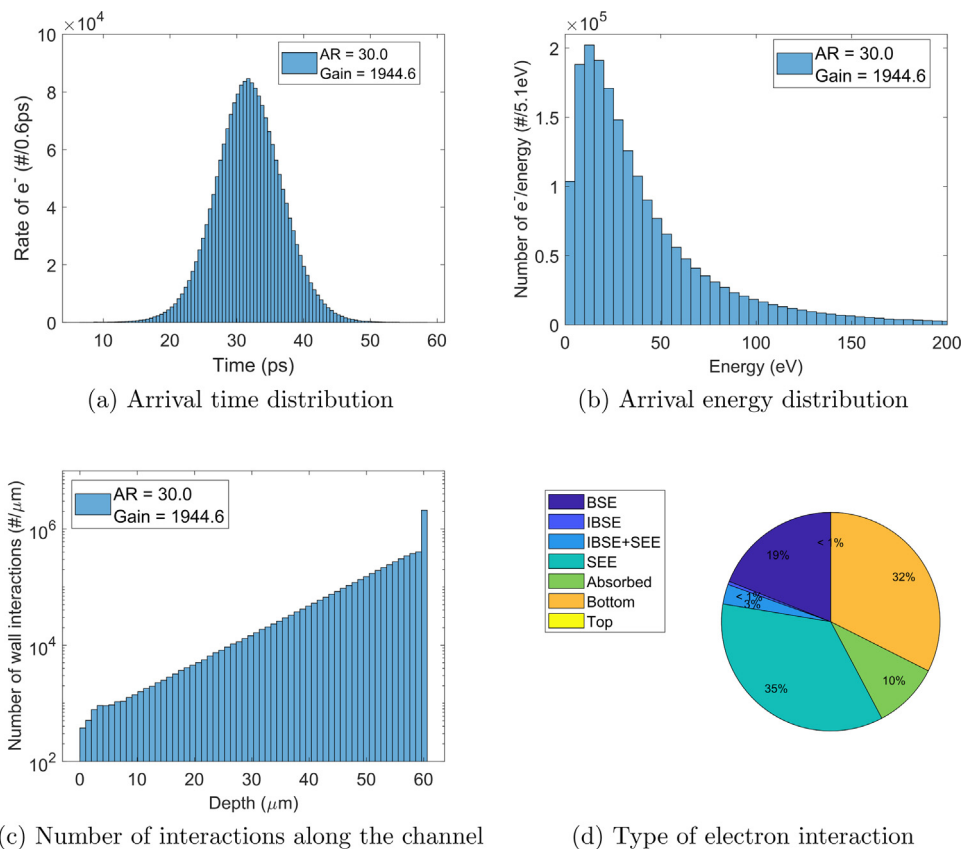


Fig. 7. Cumulative results of 1000 incident electrons in a a-Si:H AMCP channel with 60  $\mu\text{m}$  length and 2  $\mu\text{m}$  diameter. BSE = elastically backscattered electron, IBSE = inelastically backscattered electron, SEE = secondary electron, Bottom = electron arrived at the bottom of the channel, Top = electron was absorbed at the top electrode. The total number of interactions was 5'997'624.

transit time through the channel is fast, on the order of tens of ps, as expected for MCPs. The full width at half maximum (FWHM) jitter of the arrival time distribution is about 10 ps (see Fig. 7a). The arrival energy distribution of the secondary electrons at the end of the channel is shown in Fig. 7b. We observe that a majority of the electrons exit the channel with energies below 50 eV. This is consistent with experimental measurements of the electron energies at the exit of the AMCP channel of about 40 eV [24]. The number of impacts along the channel is shown in Fig. 7c and corresponds to what is expected from an electron multiplier, i.e. the number of impacts increases exponentially with increasing channel depth. In Fig. 7d, the proportions of the different types of events occurring inside the channel are shown. As expected from electron emission energy measurements, backscattering is an important contributor to the overall electron emission process.

In the following section, the AMCP response to single electrons is elaborated. To account for statistical variations, 1000 simulation runs were performed, each for a single primary electron arriving at a random height at the top of the channel with an incident angle of 30°. In Fig. 8a, the cumulative number of electrons as a function of their arrival time for each incident electron is shown. In this graph, a wide variation in gain with an average at about 2000 is observed. Consequently, the output current, plotted in Fig. 8b, shows a significant variation as well. The temporal distribution of the output current however, does not show much variation, which is crucial for time-of-flight detection. Compared to the previously calculated cumulative timing of 1000 incident electrons shown in Fig. 7a, the single electron timing distribution shows that each primary electron creates a Gaussian shaped output pulse with very similar timing distribution. To better characterize the timing variation, we calculated the current rise time in the following. From the output current, the rise time, defined in Fig. 8c as the time between 10% and 90% of the maximum current, is

calculated. The calculated rise time for all events shows a value below 10 ps, and an average of 7 ps, as observed in Fig. 8d.

In single photon detection applications, the timing jitter is another important factor that defines the timing accuracy when the origin of the detected photons is calculated in time-of-flight measurements. The timing jitter is defined as FWHM of the statistical timing distribution of the detection time. For each incident electron, the detection time is defined as the time when the number of output electrons reaches a certain threshold. Here, the threshold is defined as 80% of the average amplitude, see Fig. 8c. Alternatively, the timing jitter is defined as fractional timing, that is, the FWHM of the time distribution for reaching 80% of each current amplitude. The calculated timing jitter according to both definitions is shown in Fig. 9. The expected timing jitter is very low with 5.8 ps and 2.7 ps, according to the threshold timing jitter and fractional timing jitter definitions, respectively.

Next, the expected electron multiplication gain and timing resolution are presented here as a function of the channel diameter, the incident angle, AMCP high voltage bias and the channel length. For each set of parameters, the gain and timing resolution are calculated from 1000 simulation runs for a single primary electron.

First, the effect of different incident angles  $\theta$  (i.e. height distribution of the first interaction point according to Fig. 4) and diameters on AMCP performance were derived. The incident angle  $\theta$  was varied between 2° and 45°, and the diameter between 2  $\mu\text{m}$  and 4  $\mu\text{m}$  for a channel length of 60  $\mu\text{m}$ . The expected gain and timing jitter are shown in Fig. 10. To reach a gain of 2000, the diameter needs to be reduced to 2  $\mu\text{m}$  and the incident angle should be above 30°. According to the definition of the height of the first impact in the channel (see Fig. 4), this impact height should not be too deep inside the channel. Electrons with a flatter incidence (with respect to the channel wall) principally have a higher secondary yield. However, the first impact

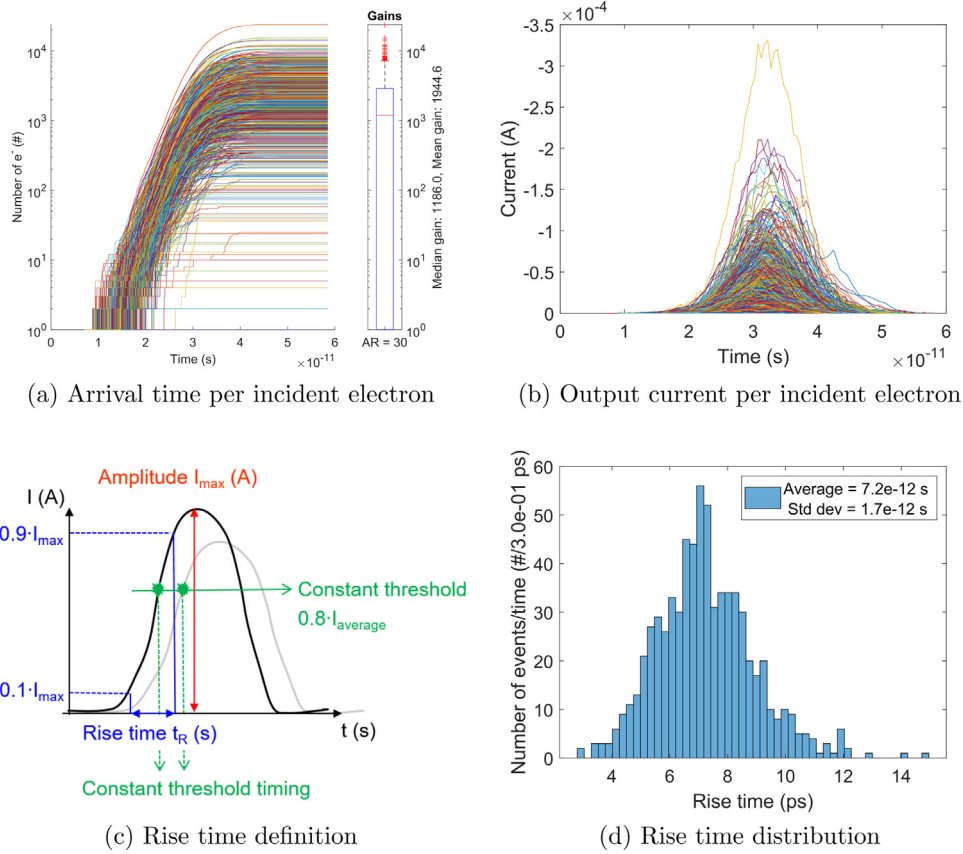


**Fig. 8.** Single electron simulation results shown for 1000 incident electrons in a a-Si:H AMCP channel with 60  $\mu\text{m}$  length and 2  $\mu\text{m}$  diameter. While the gain varies significantly for single electron detection, the timing with short rise times of 7 ps shows a small standard deviation of below 2 ps. This small temporal deviation could enable AMCPs to be used as a building block for novel time-of-flight detectors. (c) The black and the grey curve represent two different output currents, in order to indicate the rise time  $t_R$  (blue) and the constant threshold timing (green) definitions. While the green arrows indicate the constant threshold timing of two individual output currents, the threshold timing jitter is defined as the FWHM of the overall threshold timing distribution.

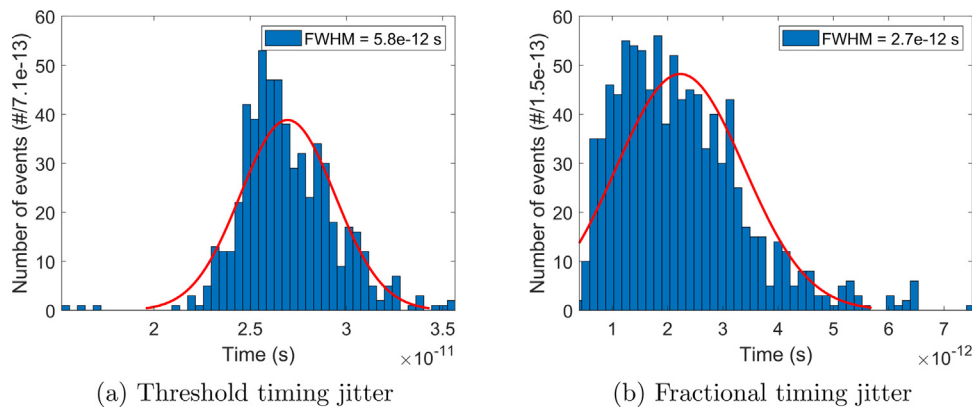


**Fig. 9.** Timing jitter of an a-Si:H AMCP channel with 60  $\mu\text{m}$  length and 2  $\mu\text{m}$  diameter.

height at the top of the channel needs to be guaranteed, e.g. by an additional magnetic field, by even smaller channel diameters or by funnel openings. As expected, the gain drops when the diameter is increased and the incident angle is reduced closer to grazing incidence on the channel wall, as in that case the primary electrons are more likely to reach deep inside the channel before their first impact. In all cases, the timing jitter is below 10 ps.

Furthermore, the gain and timing resolution for an AMCP channel of 60  $\mu\text{m}$  length were calculated using the simulation model. In this case, the AMCP diameter was varied between 2  $\mu\text{m}$  and 4  $\mu\text{m}$ , and the bias voltage between 200 V and 600 V. The results of the simulations are plotted in Fig. 11. As observed in the plots, a higher bias voltage

leads to a higher electron multiplication gain, and a lower timing jitter. Again, a significant decrease in gain with increasing diameter is observed. The variation of the gain is in the same order of magnitude as the gain, which means that for single events, a high variation of the gain is to be expected. By increasing the bias voltage, the timing jitter was further reduced. For all geometries, we observe that the fractional timing jitter is below the constant threshold timing jitter.

Finally, the model was used to optimize the AMCP dimensions. As microfabrication technology is advancing, the AMCP channel diameter could theoretically be reduced to as low as 0.5  $\mu\text{m}$ . In our simulations, the channel length was varied between 10  $\mu\text{m}$  and 30  $\mu\text{m}$  and the diameter between 1  $\mu\text{m}$  and 0.5  $\mu\text{m}$  (see Fig. 12). In addition, a maximum

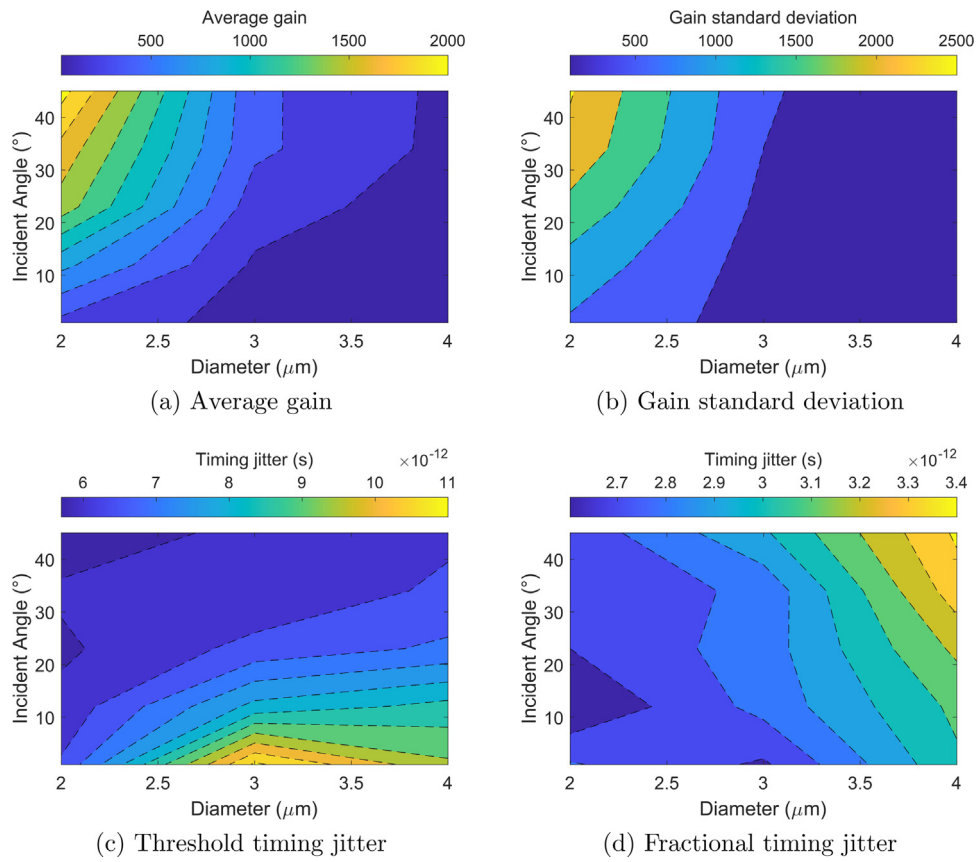


Fig. 10. Gain and timing variations with incident electron angle and channel diameter.

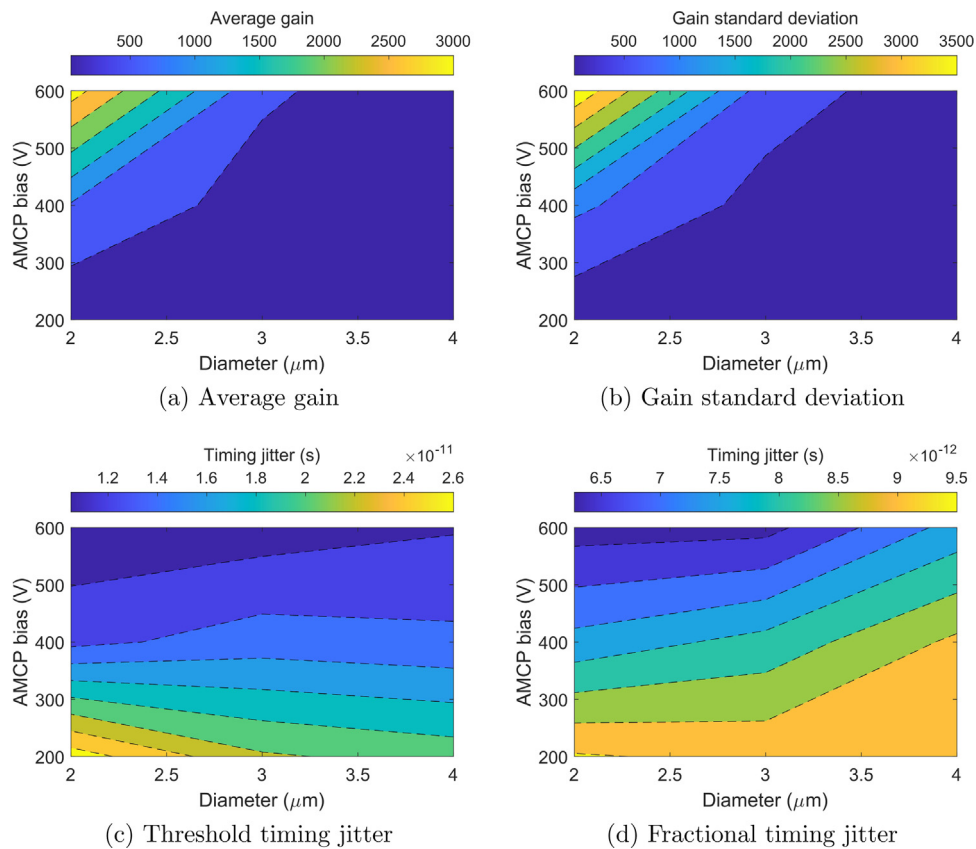


Fig. 11. Gain and timing variations with channel diameter and bias voltage.

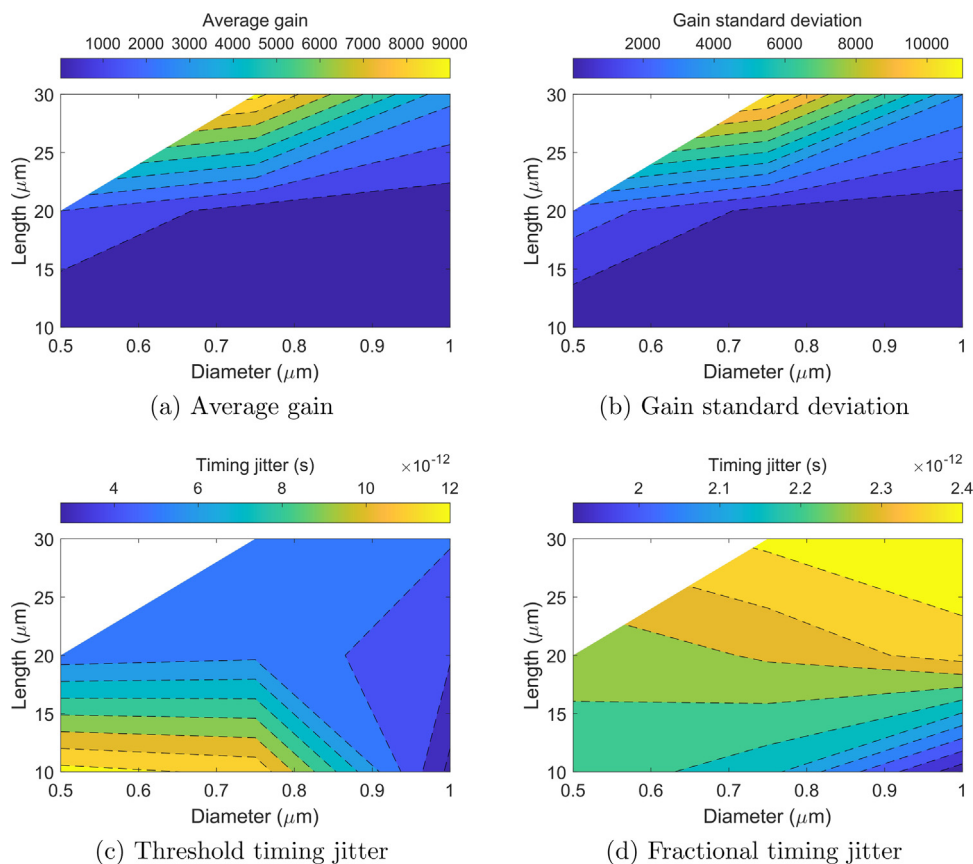


Fig. 12. Gain and timing variations for miniaturized AMCPs.

electric field of  $20 \text{ V}/\mu\text{m}$  and an incident angle of  $30^\circ$  were set. We do not show results for a channel length of  $30 \mu\text{m}$  and a diameter of  $0.5 \mu\text{m}$ , as the calculated electron gain would be above  $10^6$  according to our model. As mentioned in Section 3, pore gain saturation may be expected at such high gains and we cannot confidently predict the effective gain with the current modelling presumptions. It can be observed that the channel length should not be reduced to below  $30 \mu\text{m}$ , as the gain is very limited for shorter channels even if the maximum electric field is applied. However, the shorter channels can lead to very low timing jitter. Overall, the simulated AMCP performances are promising for single photon detection.

### 6. FEM results

As in MCPs, only the open area of an AMCP can be used for detection. Conventionally, the channel opening only covers up to a maximum of 60% of the whole area. In order to improve the collection efficiency, channels need to be fabricated with funnel openings to detect all incident electrons impinging on the AMCP. For this purpose, we present the AMCP model in a FEM framework which allows to model non-cylindrical channel shapes. Hence, the AMCP geometries can be optimized via this framework in order to achieve a maximum collection efficiency. Here, the response of an array of AMCP channels with a funnel opening for 100% collection efficiency is presented. Contrary to the kinematic model, here the electron trajectories start at a photocathode, which can lead to electrons being accelerated through a channel without hitting the channel wall. For this reason, the electron multiplication gain shown in this section might be underestimated.

Depending on the shape of the funnel opening realized by the fabrication process, the electric field profile can change, which consequently causes the electron multiplication dynamics to vary. As an example, the electric field lines for four different funnel shapes are plotted in

Fig. 13. In these plots, the electric field was modelled in 2D when a bias voltage of  $-500 \text{ V}$  was applied at the remaining top electrode and a bias voltage of  $-1 \text{ kV}$  was applied at a photocathode at  $1 \text{ mm}$  distance above the AMCP. As observed in Fig. 13a, the electric field lines in this geometry are denser compared to all the other geometries. This might lead to a stronger electron acceleration and less interactions on top of the funnels. On the other hand, in Fig. 13b and c, the electric field lines arrive perpendicular to the surface inside the funnel, which might reduce the secondary emission. In general a triangular shape as in Fig. 13d appears to be best suited for a high collection efficiency. Hence, the triangular shaped funnels were chosen to model the response to single electron incidence of a  $5 \times 5$  AMCP channel array with funnels covering 100% of the AMCP area. The geometrical setup is shown in Fig. 14a. A total channel length of  $60 \mu\text{m}$  and a funnel depth of  $10 \mu\text{m}$  was used, with a channel pitch of  $10 \mu\text{m}$ . A photocathode with a bias voltage of  $-1000 \text{ V}$  was placed  $20 \mu\text{m}$  above the array and the top edges of the funnel array were set to  $-500 \text{ V}$  while the bottom electrode was set to ground. The electron gain and the time response were calculated for 1000 cases of an incident single electron emitted from a random position on the photocathode. In Fig. 14b, the collected electrons and their arrival times are shown. As for single channels the time response is very fast, and the signal rise time is below  $10 \text{ ps}$  (see Fig. 14d). On the other hand, a lower average gain was calculated compared to straight AMCP channels. This could be due to the fact that in the single-channel model the first interaction of the primary electron was fixed in the upper part of the channel. For the present simulation of funnel AMCPs, the primary electron is accelerated parallel to the channel and may not interact with the channel wall at all and hit the channel exit without producing secondary electrons. While the present simulation is more realistic than the single channel model in terms of electrons being generated at a photocathode, geometrical imperfections in a real device would reduce the likelihood of non-interacting electrons compared to the idealized simulation.

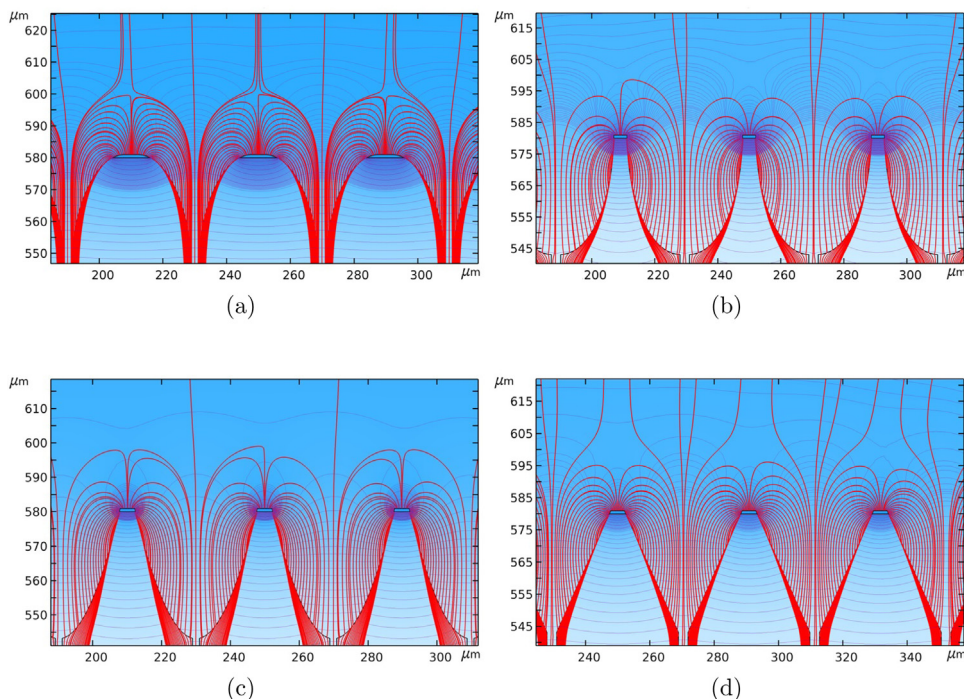


Fig. 13. Electric field lines (red) and equipotential lines (grey) for different funnel openings of AMCP channels: convex oval funnels (a), concave oval funnels (b), concave parabolic funnels (c), triangular funnels (d).

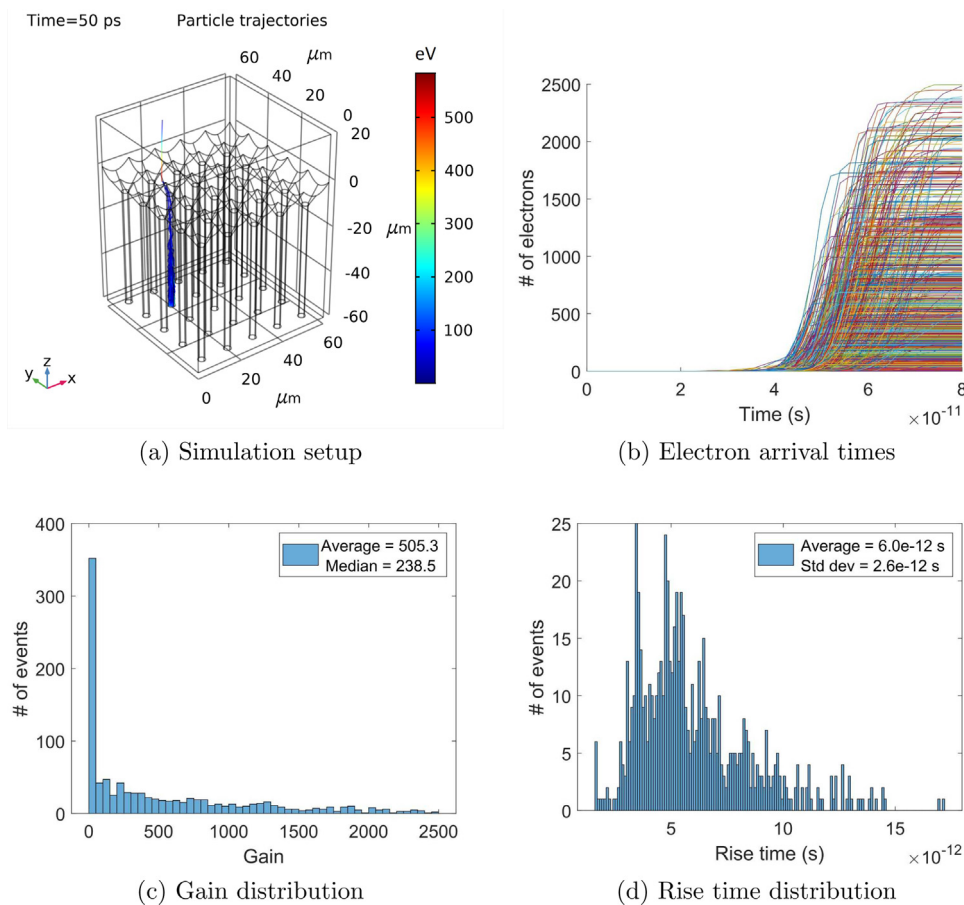


Fig. 14. The response of single electron incidence on an array of AMCPs with triangular funnel openings calculated with the finite element model. The average gain of 505 is reduced by a factor of 4 compared to straight channels, while the signal rise time is comparable to straight channels. However, here the collection efficiency is close to 100%.

## 7. Conclusion and outlook

The AMCP simulation models presented here facilitate the optimization of AMCPs while allowing for an evaluation of their characteristics as single-photon detectors. The AMCP channel geometries currently developed benefit from a timing jitter of 2.7 ps which is lower than for most available single photon detectors. These values are very promising for applications in TOF PET detectors where the timing resolution is currently limited to a few tens of ps relative to the goal of having jitters below 10 ps [25].

Similar to MCPs, the future prospects for AMCPs depend heavily on the advancement of readout electronics, since AMCPs are only one element of an assembly that integrates AMCPs and electronic readout devices. The current advancement of readout electronics for MCPs has been critical to expanding the applications of MCPs as photon counters [26]. Since the readout electronics will be integrated monolithically with AMCPs, there is no need to operate at high gains of  $10^6$ , as in conventional MCP detectors. Therefore modelling of AMCP operation in non-saturated mode, as done in this paper, is sufficient for most foreseen applications of AMCP amplifiers.

In this paper, we presented results exclusive to AMCPs without an additional coating, using the secondary emission characteristics of bare a-Si:H. Although a highly emissive coating has the potential to increase the electron multiplication gain tremendously, further AMCP measurements are necessary to confirm this. Based on our simulation results, the gain of bare AMCPs could already be sufficient for detecting single photons, as long as higher bias voltages are applied. However, applying higher bias voltages may increase the design complexity and the leakage current. Additionally, as indicated by the simulations and the measurements, highly emissive coatings could substantially improve the gain and eliminate the need for a high gain low noise amplifier in the readout electronics. Consequently, this reduces the design complexity, increases the pixel density and decreases the power consumption of the integrated detector.

From the simulation results, it can be deduced that the length of the AMCP channels should be above 30  $\mu\text{m}$ . In shorter channels, a sufficiently high voltage for producing a sufficient amount of secondary electrons for the detection of single photons cannot be sustained by the device. Following the results, we consider an optimal AMCP channel length to be about 50  $\mu\text{m}$  and above. Depending on the electronic readout, a minimum AR of at least 25 is necessary with length and diameter depending on the application. This is a very promising result as experimentally AMCPs can be realized with aspect ratios of up to 50. With a certain aspect ratio channel a higher gain can be reached with longer channels, when the maximum electric field is applied. For TOF applications on the other hand a minimum channel diameter of 1  $\mu\text{m}$  can be used to minimize timing jitter. According to the secondary yield parameters used, AMCP gain is decreasing for channel diameters below 1  $\mu\text{m}$ , as electrons are not accelerated to high enough energies in between impacts to create a sufficient number of secondary electrons.

Another important observation is that the timing resolution of AMCPs is not affected by a funnel opening. This means that by adding funnels on top of the channels we can substantially increase the collection efficiency without deteriorating the timing jitter. However, our prediction of a lower gain of funnel shaped AMCPs might be misleading due to discrepancy between the real device geometry (rough channel surface, non uniform or non parallel electric fields, etc.) and the simulated geometries.

The models presented in this work can be used to further optimize the channel shapes, fill factor, inhomogeneous electric field, location of the intermediate electrodes, and many other design parameters. In particular, the FEM can be used to predict the influence of a magnetic field on AMCP performance, for the use of AMCP-based detectors in combined clinical magnetic resonance and TOF PET detection systems. Future developments of the simulation models might include incorporation of charging effects on the electrical field and secondary emission

yield. Such an addition would help to predict the response of highly emissive AMCP channels, as well as channels under high electric fields, with greater accuracy. Overall, the results of our simulations confirm that the current geometry of AMCP channels with a 60  $\mu\text{m}$  length and 2  $\mu\text{m}$  diameter is a sound basis for developing an ultrafast detector, with a gain above 2000 and a very low timing jitter of just a few ps, making these designs suitable for single-photon detection.

## CRediT authorship contribution statement

**Janina Löffler:** Conceptualization, Writing – original draft, Writing – review & editing, Methodology, Software, Validation, Formal analysis, Investigation. **Jonathan Thomet:** Conceptualization, Writing – review & editing, Visualization, Software. **Samira Frey:** Validation, Software, Formal analysis, Investigation. **Christophe Ballif:** Supervision. **Nicolas Wyrsh:** Conceptualization, Writing – review & editing, Supervision, Project administration, Funding acquisition.

## Declaration of competing interest

The authors declare that they have no known competing financial interests or personal relationships that could have appeared to influence the work reported in this paper.

## Acknowledgments

Results presented here were obtained with the financial support of the Swiss National Science Foundation project 200021\_162525/1. We would like to thank Dr. Anton Tremsin for sharing his valuable insights into MCP modelling, the Comsol support team, as well as Dr. Stefan Gundacker, and our colleagues and collaborators from the Sinergia project and from PV-lab, especially Mohammad Beygi and Daniel Jacobs for proofreading and substantially improving the manuscript.

Swiss National Science Foundation through the Sinergia program (Grant No. 177165, 2018–2022).

## References

- [1] A. Franco, J. Geissbühler, N. Wyrsh, C. Ballif, Fabrication and characterization of monolithically integrated microchannel plates based on amorphous silicon, *Sci. Rep.* 4 (August 2015) (2014) 1–7, <http://dx.doi.org/10.1038/srep04597>, URL: <http://www.nature.com/doifinder/10.1038/srep04597>.
- [2] J. Löffler, C. Ballif, N. Wyrsh, Amorphous silicon-based micro-channel plate detectors with high multiplication gain, *Nucl. Instrum. Methods Phys. Res. A* (2018) <http://dx.doi.org/10.1016/j.nima.2017.12.036>.
- [3] G. Bertuccio, S. Caccia, Progress in ultra-low-noise ASICs for radiation detectors, *Nucl. Instrum. Methods Phys. Res. A* 579 (1) (2007) 243–246, <http://dx.doi.org/10.1016/j.nima.2007.04.042>.
- [4] P. Lecoq, Pushing the limits in time-of-flight PET imaging, *IEEE Trans. Radiat. Plasma Med. Sci.* 1 (6) (2017) 473–485, <http://dx.doi.org/10.1109/trpms.2017.2756674>.
- [5] L. Giudicotti, Time dependent model of gain saturation in microchannel plates and channel electron multipliers, *Nucl. Instrum. Methods Phys. Res. A* 659 (1) (2011) 336–347, <http://dx.doi.org/10.1016/j.nima.2011.07.017>.
- [6] A.S. Tremsin, H.F. Lockwood, D.R. Beaulieu, N.T. Sullivan, E. Munro, J. Rouse, 3D microscopic model of electron amplification in microchannel amplifiers for maskless lithography, *Physics Procedia* 1 (1) (2008) 565–572, <http://dx.doi.org/10.1016/j.phpro.2008.07.139>.
- [7] C.A. Kruschwitz, M. Wu, G.A. Rochau, Monte Carlo simulations of microchannel plate detectors. II. Pulsed voltage results, *Rev. Sci. Instrum.* 82 (2) (2011) <http://dx.doi.org/10.1063/1.3530451>.
- [8] A.V. Shymanska, V.A. Babakov, Fast Monte Carlo method in stochastic modelling of charged particle multiplication, *Int. J. Appl. Phys. Math.* 5 (3) (2015) 218–226, <http://dx.doi.org/10.17706/ijapm.2015.5.3.218-226>, URL: <http://www.ijapm.org/show-57-492-1.html>.
- [9] M.A. Furman, M.T. Pivi, Probabilistic model for the simulation of secondary electron emission, *Phys. Rev. Spec. Top. - Accel. Beams* 5 (12) (2002) 82–99, <http://dx.doi.org/10.1103/PhysRevSTAB.5.124404>.

- [10] J. Löffler, Towards Single Photon Detection with Amorphous Silicon Based Microchannel Plates, (Ph.D. thesis), EPFL, 2021.
- [11] J. Cazaux, Reflectivity of very low energy electrons (< 10 eV) from solid surfaces: Physical and instrumental aspects, *J. Appl. Phys.* 111 (6) (2012) 064903, <http://dx.doi.org/10.1063/1.3691956>, URL: <http://aip.scitation.org/doi/10.1063/1.3691956>.
- [12] J. Cazaux, Calculated influence of work function on SE escape probability and secondary electron emission yield, *Appl. Surf. Sci.* 257 (3) (2010) 1002–1009, <http://dx.doi.org/10.1016/j.apsusc.2010.08.007>.
- [13] J. Kawata, K. Ohya, K. Nishimura, Simulation of secondary electron emission from rough surfaces, *J. Nucl. Mater.* 220–222 (1995) 997–1000, [http://dx.doi.org/10.1016/0022-3115\(94\)00460-9](http://dx.doi.org/10.1016/0022-3115(94)00460-9).
- [14] J. Pierron, C. Inguibert, M. Belhaj, J. Puech, M. Raine, Effect of rectangular grooves and checkerboard patterns on the electron emission yield, *J. Appl. Phys.* 124 (9) (2018) <http://dx.doi.org/10.1063/1.5028216>.
- [15] G. Troncoso, J.M. García-Martín, M.U. González, C. Morales, M. Fernández-Castro, J. Soler-Morala, L. Galán, L. Soriano, Silver nanopillar coatings grown by glancing angle magnetron sputtering for reducing multipactor effect in spacecrafts, *Appl. Surf. Sci.* 526 (May) (2020) 146699, <http://dx.doi.org/10.1016/j.apsusc.2020.146699>.
- [16] J. Cazaux, E-induced secondary electron emission yield of insulators and charging effects, *Nucl. Instrum. Methods Phys. Res. B* 244 (2) (2006) 307–322, <http://dx.doi.org/10.1016/j.nimb.2005.10.006>.
- [17] M. Belhaj, T. Tondou, V. Inguibert, P. Barroy, F. Silva, A. Gicquel, The effects of incident electron current density and temperature on the total electron emission yield of polycrystalline CVD diamond, *J. Phys. D: Appl. Phys.* 43 (13) (2010) <http://dx.doi.org/10.1088/0022-3727/43/13/135303>.
- [18] J. Ladislav Wiza, Microchannel plate detectors, *Nucl. Instrum. Methods* 162 (1) (1979) 587–601, [http://dx.doi.org/10.1016/0029-554X\(79\)90734-1](http://dx.doi.org/10.1016/0029-554X(79)90734-1), URL: <https://www.sciencedirect.com/science/article/pii/0029554X79907341>.
- [19] Z. Insepov, V. Ivanov, J. Elam, B. Adams, H. Frisch, Charge relaxation and gain depletion for candidate secondary electron emission materials, in: IEEE Nuclear Science Symposium Conference Record, vol. 2, 2010, pp. 1193–1198, <http://dx.doi.org/10.1109/NSSMIC.2010.5873957>.
- [20] A. Franco, Monolithic Particle Detectors based on Hydrogenated Amorphous Silicon (Ph.D. thesis), EPFL, 2014, p. 180, <http://dx.doi.org/10.5075/epfl-thesis-6290>, URL: <https://infoscience.epfl.ch/record/200863>.
- [21] J.R.M. Vaughan, A new formula for secondary electron emission yield, *IEEE Trans. Electron Devices* 36 (9) (1989) 1963–1967, <http://dx.doi.org/10.1109/16.34278>.
- [22] S.J. Jokela, I.V. Veryovkin, A.V. Zinovev, J.W. Elam, A.U. Mane, Q. Peng, Z. Insepov, Secondary electron yield of emissive materials for large-area microchannel plate detectors: Surface composition and film thickness dependencies, *Physics Procedia* 37 (2012) 740–747, <http://dx.doi.org/10.1016/j.phpro.2012.03.718>, URL: <http://linkinghub.elsevier.com/retrieve/pii/S1875389212017567>.
- [23] V. Ivanov, A. Barnyakov, M. Barnyakov, Calibration procedure in microchannel amplifiers design, *Nucl. Instrum. Methods Phys. Res. A* 903 (June) (2018) 170–174, <http://dx.doi.org/10.1016/j.nima.2018.05.046>.
- [24] S. Frey, J. Löffler, C. Ballif, N. Wyrsh, Characterization of amorphous silicon based microchannel plates with high aspect ratio, in: 2019 IEEE Nuclear Science Symposium and Medical Imaging Conference, NSS/MIC 2019, Institute of Electrical and Electronics Engineers Inc., 2019, <http://dx.doi.org/10.1109/NSS/MIC42101.2019.9059714>.
- [25] S. Gundacker, R. Martínez Turtos, N. Kratochwil, R.H. Pots, M. Paganoni, P. Lecoq, E. Auffray, Experimental time resolution limits of modern SiPMs and TOF-PET detectors exploring different scintillators and cherenkov emission, *Phys. Med. Biol.* 65 (2) (2020) ab63b4, <http://dx.doi.org/10.1088/1361-6560/ab63b4>.
- [26] A.S. Tremsin, J.V. Vallerga, O.H.W. Siegmund, J. Woods, L.E. De Long, J.T. Hastings, R.J. Koch, S.A. Morley, Y.-D. Chuang, S. Roy, Photon-counting MCP/Timepix detectors for soft X-ray imaging and spectroscopic applications, *J. Synchrotron Radiat.* 28 (4) (2021) 1069–1080, <http://dx.doi.org/10.1107/s1600577521003908>.